ADVANCED MATERIALS
www.advmat.de

A BF_3-Doped MXene Dual-Layer Interphase for a Reliable Lithium-Metal Anode

*Mingwei Shang, Osman Goni Shovon, Francis En Yoong Wong, and Junjie Niu**

A dual-layer interphase that consists of an in-situ-formed lithium carboxylate organic layer and a thin BF_3-doped monolayer Ti_3C_2 MXene on Li metal is reported. The honeycomb-structured organic layer increases the wetting of electrolyte, leading to a thin solid electrolyte interface (SEI). While the BF_3-doped monolayer MXene provides abundant active sites for lithium homogeneous nucleation and growth, resulting in about 50% reduced thickness of inorganic-rich components among the SEI layer. A low overpotential of less than 30 mV over 1000 h cycling in symmetric cells is received. The functional BF_3 groups, along with the excellent electronic conductivity and smooth surface of the MXene, greatly reduce the lithium plating/stripping energy barrier, enabling a dendrite-free lithium-metal anode. The battery with this dual-layer coated lithium metal as the anode displays greatly improved electrochemical performance. A high capacity-retention of 175.4 mAh g^{-1} at 1.0 C is achieved after 350 cycles. In a pouch cell with a capacity of 475 mAh, the battery still exhibits a high discharge capacity of 165.6 mAh g^{-1} with a capacity retention of 90.2% after 200 cycles. In contrast to the fast capacity decay of pure Li metal, the battery using NCA as the cathode also displays excellent capacity retention in both coin and pouch cells. The dual-layer modified surface provides an effective approach in stabilizing the Li-metal anode.

1. Introduction

In order to meet the energy demand in ever growing electric vehicles (EVs) and portable electronics, high-energy-density lithium-ion batteries (LIBs) are required. Due to its high specific capacity of 3860 mAh g^{-1}, the lowest working potential of −3.04 V, and metallic conductivity, lithium metal is considered as one of the most promising anodes in next-generation LIBs.[1] However, its high chemical activity leads to complex reaction with electrolyte, which forms un-uniform solid electrolyte interface (SEI) on the surface.[2,3] In addition to the continuous consumption of both lithium and electrolyte, the non-homogeneous nucleation/growth generates lithium dendrites, which poses big challenges on the battery failure and safety concerns.[4–6]

To date, various strategies have been applied to inhibit the growth of lithium dendrites, including optimizing electrolyte,[7,8] constructing artificial SEI,[9,10] applying protective coating layer,[11,12] introducing lithiophilic seeds,[13] designing 3D nano structures,[14] and others.[15,16] A controlled nucleation and orientated growth of lithium can suppress the growth of dendrites.[17] Recently 2D MXene has been attracting more and more attention in batteries due to its high conductivity, high stability, and layered structure.[18,19] It has been widely used as a host for various novel electrode materials in LIBs such as GeO_x@MXene[20] and Si@MXene.[21–23] The superior conductivity, special layered structure, and adjustable functional groups make it a promising candidate as a lithium hosting material.[24,25] Zhang et al. constructed parallelly aligned MXene layer on the surface of lithium metal, leading to a horizontal growth of lithium on the surface of MXene.[20] Vertically aligned MXene nanosheets were also used as a host in a lithium-metal electrode.[26] To achieve a lithiophilic surface, typically active sites were introduced on the MXene surface, which promoted the homogeneous nucleation and growth of lithium. Single zinc atoms and ultrafine Au layer immobilized on MXene layers were produced to efficiently induce Li nucleation/growth.[25,27] In parallel, a reliable hybrid anode material $LiTiO_2$–Li_3N–C was synthesized by a high-temperature pyrolysis of Ti_3C_2 MXene in NH_3/Ar, where the Ti_3C_2 was transferred into carbon-based material.[28] Another strategy is to transfer Ti_3C_2 into TiO_2@C by calcination, where the formed carbon can provide electronic conductivity while the TiO_2 nanoparticles serves as active sites to accommodate the volume change during lithium plating and stripping.[24,29]

The design of an artificial interface layer on lithium-metal surface also showed improvements for lithium plating and stripping. In our previous work, we designed an inter-layer-calated thin Li-metal electrode using non-delaminated $Ti_3C_2T_x$ MXene stacks coated on a Li-metal host, which greatly reduced the dead lithium and electrolyte consumption by forming a thin SEI layer.[30] Recent study shows that a protective layer by combining organic and inorganic layers can achieve rapid Li-ion diffusion, high mechanical stability, and better flexibility.[11] In this article, we developed an ultrathin dual-layer interphase that

M. Shang, O. G. Shovon, F. E. Y. Wong, J. Niu
Department of Materials Science and Engineering
CEAS
University of Wisconsin–Milwaukee
Milwaukee, WI 53211, USA
E-mail: niu@uwm.edu

The ORCID identification number(s) for the author(s) of this article can be found under https://doi.org/10.1002/adma.202210111.

DOI: 10.1002/adma.202210111

consists of an in-situ-formed lithium carboxylate organic layer and a BF_3-doped monolayer Ti_3C_2 MXene (BF_3-MXene) on the Li-metal surface via a wet-chemical method. The pre-formed honeycomb-like organic layer as an artificial SEI layer stabilizes the Li-metal surface. The BF_3-MXene layer further enhances the interfacial stability between the MXene surface and electrolyte.[31] In parallel, the large MXene surface with functional groups exhibited high lithiophilicity and excellent electronic conductivity which greatly reduced the lithium plating/stripping energy barrier, enabling a dendrite-free lithium-metal anode. As the result, the designed Li-metal battery demonstrated a high-capacity retention after 500 cycles at 1.0 C when paired with NMC811 as cathode, which is much higher than the untreated Li-metal battery. The improved cycling performance of high-capacity pouch cell batteries was also achieved, displaying great potential in large-energy-density batteries.

2. Results and Discussions

The dual-layer coated lithium metal (D-Li) was constructed through a facile coating approach, as shown in **Figure 1**a. The first lithium carboxylate layer was in situ formed on the Li-metal surface by reacting with pentanoic acid. Due to the participation of carboxylic acid, the formed layer has similar organic components to the naturally formed SEI,[32] which is considered as a thin artificial SEI layer. In addition, the existing plenty of carboxyl and hydroxyl groups lead to an intimate contact between the MXene nanosheet and the Li-metal surface.[33] To prepare the second layer, multilayer Ti_3C_2 MXene was first obtained after etching MAX precursor by HF acid. The morphology and crystallographic orientation were confirmed by using scanning electron microscopy (SEM) (Figure S1a, Supporting Information) and X-ray diffraction (Figure S1b, Supporting Information), respectively. Subsequently MXene monolayer nanosheets were received in tetrahydrofuran (THF) after a series of treatments including further HF acid etching, intercalation, sonication, and centrifuge.[30,34] It was found that the monolayer suspension still remained homogeneous mixture after 5 min while the multilayer suspension became transparent (Figure S2a,b, Supporting Information). After mixing with pre-treated BF_3 in THF, the monolayer MXene dispersion was coated on the lithium carboxylic layer by using dip or spray coating. Thus a dual-layer interphase composed of an artificial SEI layer and an inorganic BF_3-MXene layer was formed on the Li metal.

The surface morphology evolution of the Li metal with different layers was investigated by using SEM. Compared to the smooth surface of pure Li (Figure 1b), a honeycomb-like rough surface with plenty of nano-flakes was found after pentanoic acid treatment (Figure 1c), which largely increased the surface area. The monolayer BF_3-MXene then filled up the rough

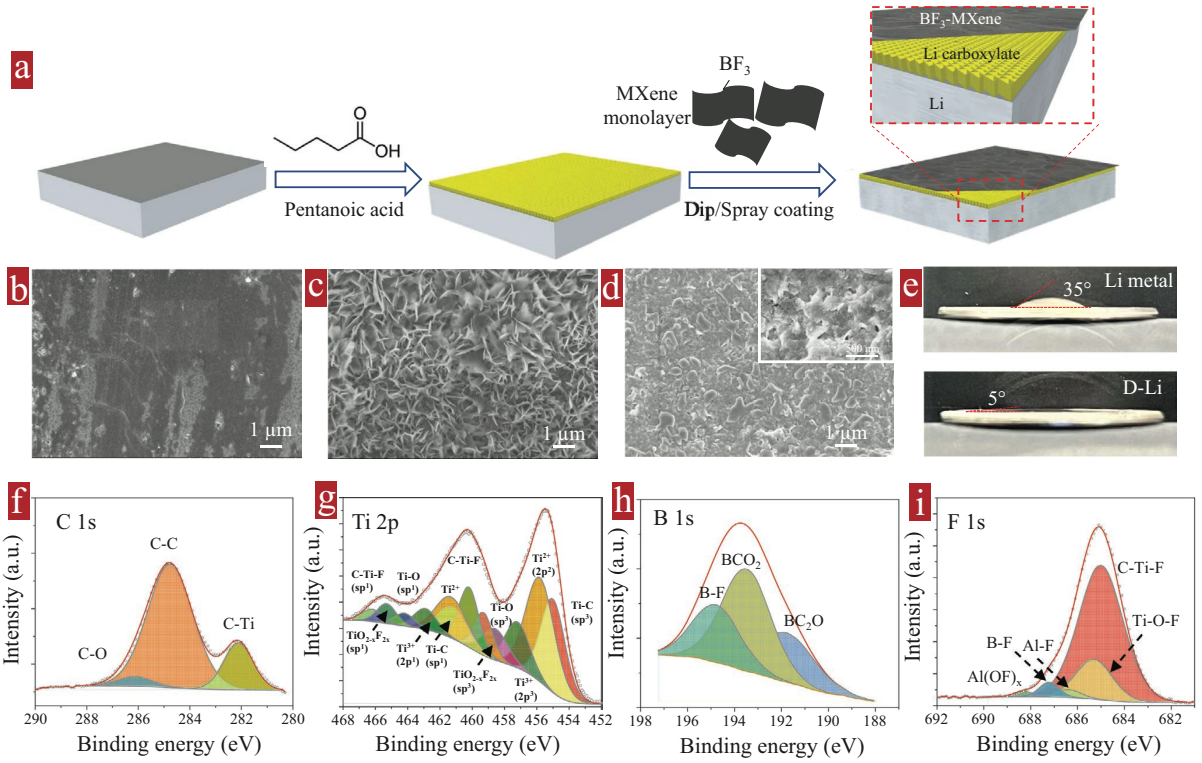

Figure 1. Design dual-layer coated Li-metal anode. a) Schematic illustration of designing D-Li using BF_3-doped Ti_3C_2 MXene. b–d) SEM morphologies of original Li metal (b), after pentanoic acid (c), and BF_3-MXene (d) treatments. The inset in (d) is an enlarged morphology. e) Contact angles of electrolyte on pure Li metal (top) and D-Li (bottom). f–i) XPS spectra of C 1s (f), Ti 2p (g), B 1s (h), and F 1s (i) of the as-received BF_3-MXene.

lithium carboxylate layer, enabling a close contact with Li metal (Figure 1d). The electrolyte wettability of the surface was also checked. As seen in Figure 1e, a high contact angle of 35° with pure Li metal was obtained while a drastically deceased contact angle of 5° was measured with the dual-layer coated Li metal. The reduced contact angle indicates an enhanced uniform distribution of Li ions in the interface, which might be originated from the better lithiophilic property of the doped MXene layer.[35]

The chemical composition of different samples was analyzed by X-ray photoelectron spectroscopy (XPS). As seen in Figure S3a,d, Supporting Information, the peak intensity of Li_2CO_3/LiOH and Li_2O was largely reduced after pentanoic acid treatment. It can also be observed from the peak variation of C 1s (Figure S3b,e, Supporting Information) and O 1s (Figure S3c,f, Supporting Information). The appeared new peak at 54.8 eV confirmed the presence of lithium carboxylate ($ROCO_2Li$) (Figure S3d, Supporting Information), which can serve as an artificial SEI layer to regulate the lithium deposition and extraction and thus to suppress the dendrite.[32] After forming the dual-layer architecture, the F 1s and B 1s peaks related to carbon and titanium bindings from MXene were detected, showing the success doping BF_3 in MXene matrix (Figure S3g–l, Supporting Information). To exclude the interference from the organic salt, the XPS spectra of BF_3-MXene were also analyzed (Figure 1f–i and Figure S4, Supporting Information). Three C 1s peaks at 282.0, 284.8, and 286.2 eV were found, which correspond to C—Ti, C—C, and C—O, respectively (Figure 1f).[36] Compared with the sample without MXene (Figure S5, Supporting Information), two large peaks emerged at 191.8 and 193.5 eV that correspond to BC_2O and BCO_2 (Figure 1h),[37,38] which originated from the binding between the doped BF_3 and MXene. In addition, the enhanced F 1s peaks centered at 685.0 eV (Figure 1i) that are referred to C—Ti—F and Ti—O—F also demonstrate the doped element in MXene. The other peaks of Ti 2p (Figure 1g) and O 1s (Figure S4, Supporting Information) were from the MXene.[39] The doped monolayer MXene facilitates the uniform lithium deposition horizontally on the surface, while the existing B and F dopings can further reduce the lithium nucleation barrier, thus avoiding dendrite growth.[37]

Figure 2 shows the electrodeposition morphology evolution of pure Li and D-Li at a current density of 0.2 mA cm^{-2} after plating 1, 2, 5, 10, and 20 h, respectively. As observed from the pure Li (Figure 2a,b), lithium stone bumps with a size of ≈1 µm started to appear at 2 h with a capacity of 0.4 mAh cm^{-2}. With longer plating time of over 5 h, the bumps grew larger than 5 µm. As a result, the uneven growth of lithium led to generate lithium dendrites and defects.[3,37,40] For the D-Li sample, we found the lithium started to deposit on the MXene within 2 h (Figure 2c). Due to the larger surface area and numerous nucleation sites provided by the BF_3-MXene, the surface was uniformly covered by lithium. The initially formed small pores were gradually filled up when the plating time reached over 5 h (Figure 2d and Figure S6a,b, Supporting Information). After 10 h plating, a dense, smooth lithium film was formed. Even after 20 h deposition (4 mAh cm^{-2}), the homogeneous surface with zero dendrite or mossy lithium still remained (Figure 2d). Under high current density of 1.0 and

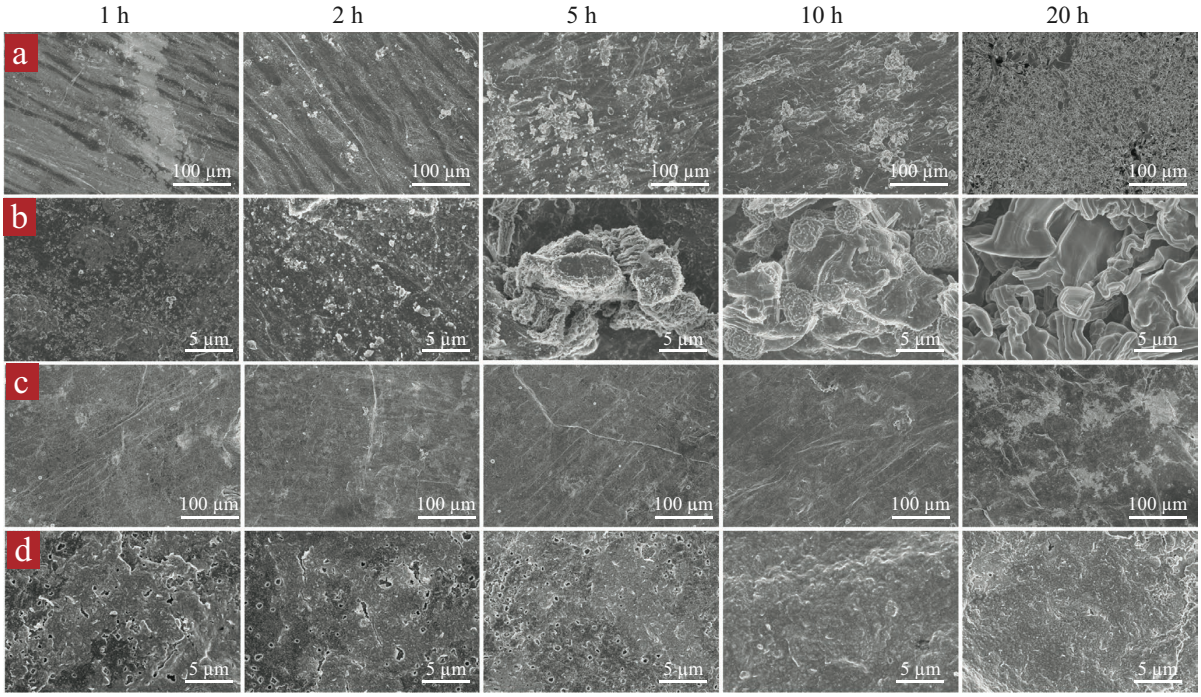

Figure 2. Surface morphology evolution of anode electrodes after plating in symmetric cells. a–d) SEM morphologies of pure Li metal at low-magnification (a) and high-magnification (b) and D-Li at low-magnification (c) and high-magnification (d) under a current density of 0.2 mA cm^{-2} after plating for 1, 2, 5, 10, and 20 h.

2.0 mA cm^{-2}, D-Li still exhibited a relative smooth surface with free mossy/dendritic lithium formation after 10 h (Figure S7, Supporting Information). The monolayer MXene along with the honeycomb-like carboxylate provides plenty of nucleation sites for lithium deposition. In parallel, the doped functional groups containing B and F further stabilize the SEI by suppressing the growth of lithium dendrites.[31,37] To better understand the lithium dendrite prevention, mossy/dendritic Li growth/depletion upon lithium plating and stripping inside a capillary cell was observed real time. During the plating (0–40 min) and stripping (40–80 min) on D-Li at 5 mA cm^{-2}, homogeneous Li deposition/depletion without any mossy/dendritic lithium was observed (Figure S8a, Supporting Information). However, clear mossy/dendritic Li was found on the pure Li-metal surface only after plating for 5 min (Figure S8b, Supporting Information). These irreversible mossy/dendritic Li kept growing larger with long plating time. The smooth lithium deposition/depletion on D-Li further demonstrates a better mossy/dendritic lithium suppression due to the regulation of the designed dual-layer configuration.

It is known that SEI layer plays a critical role on lithium-metal deposition.[41] Here the chemical composition and element distribution of the SEI layer of the battery upon stripping after cycling were revealed via XPS depth profiles. Two C 1s peaks at 286.7 and 287.8 eV and the O 1s peak at 530.4 eV are attributed to the presence of C—O and C=O groups on the surface (**Figure 3**a,c and Figure S9a,b, Supporting Information). Also the C 1s peak at 290.6 eV and the F 1s peak at 688.5 eV demonstrated the existing —CF_3 on the surface (Figure 3a,b and Figure S9a,c, Supporting Information). It is found that the —CF_3 only appeared on the top surface of D-Li while it was still detected on pure Li metal after 60 s etching (about 18 nm in depth), which indicates a much thicker organic-rich layer was generated on pure Li metal. After etching the D-Li for 120 s (about 36 nm), Ti—C peak at 282.1 eV (Figure 3a), Ti—O peak at 529.8 eV (Figure 3c), and intensified Ti 2p peaks (Figure 3e) were measured, confirming the coated MXene layer. As observed in Figure 3f, the deconvoluted B 1s peaks at 191.8, 193.4, and 194.8 eV that correspond to BC_2O, BCO_2, and B-F depict a successful doping of BF_3 into the MXene. The doped boron bonded to MXene may introduce more lithiophilic active sites for lithium nucleation.[38] Inorganic compounds LiF, Li_2CO_3/LiOH, and Li_2O were detected from the Li 1s spectra (Figure 3d and Figure S9d, Supporting Information). The atomic/mole ratios of lithium metal versus etching depth were calculated from the XPS depth profiles (Table S1, Supporting Information). The thickness of inorganic-rich component was estimated when the lithium metal is less

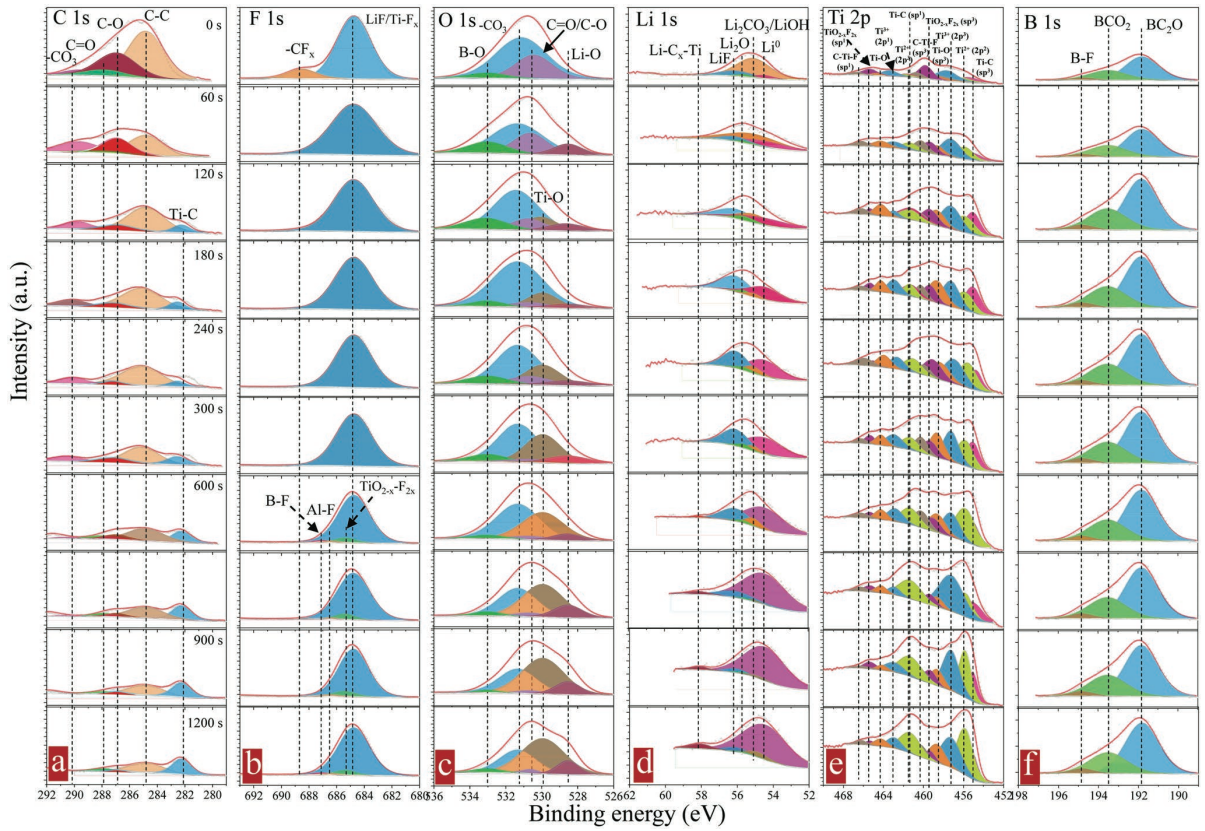

Figure 3. XPS depth profiles of the D-Li upon stripping after six cycles in a symmetric cell. a–f) Depth profiles of C 1s (a), F 1s (b), O 1s (c), Li 1s (d), Ti 2p (e), and B 1s (f). The current density and specific capacity are 1.0 mA cm^{-2} and 1.0 mAh cm^{-2}.

than 60 mol%.[30] It was found that the D-Li showed a thin inorganic-rich layer of about 135 nm while the pure Li metal had a double-sized thickness of ≈270 nm. The largely reduced inorganic-rich layer in SEI indicates much less electrolyte consumption.

Electrochemical stability of the Li-metal electrode upon lithium plating and stripping was checked by symmetric cells. It is found that both pure Li metal and D-Li cells displayed initial overpotentials of ≈51.9 and 57.5 mV and stabilized at a similar overpotential of ≈28.7 mV within the first 10 h at a current density of 1.0 mA cm^{-2} (**Figure 4**a,c). The D-Li cell maintained a low overpotential of less than 33.3 mV over 1000 h cycling (Figure 4a). As comparison, the overpotential of the pure Li-metal cell increased rapidly after about 270 h. Also a sharp peak uptake due to short circuit was observed (dashed circles in Figure 4d). Under a higher current density of 5 mA cm^{-2}, the cell with D-Li still showed a low overpotential of ≈80.2 mV after 1000 h while the cell with pure Li metal only ran 40 h before short circuit (Figure 4a). Lithium nucleation overpotential can be obtained from the voltage difference between the top and platform curves.[38] As shown in Figure 4b, the D-Li cell showed a nucleation overpotential of 51.9 mV, which is much smaller than the pure Li metal of 96.2 mV. The smaller nucleation overpotential with D-Li due to the created abundant lithiophilic sites by the doped BF_3 in MXene matrix might largely reduce the dendrite formation.[38] Cycling capability of full cell batteries paired with $LiNi_{0.8}Mn_{0.1}Co_{0.1}O_2$ (NMC811) as cathode material was measured (Figure 4e). The battery with pure Li metal delivered an initial discharge capacity of 191.9 mAh g^{-1} with Coulombic efficiency (CE) of 80.9% at 0.1 C (black). The

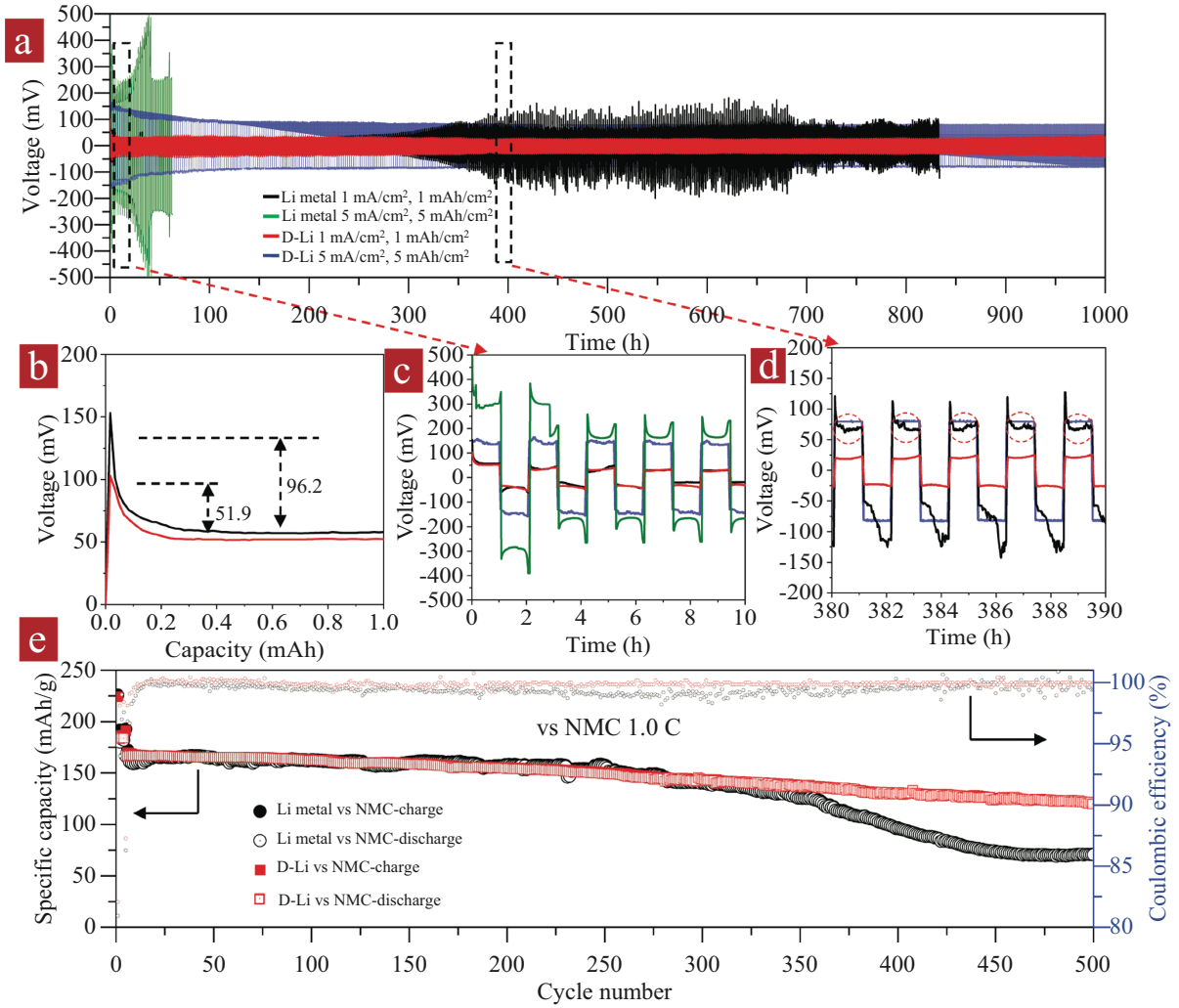

Figure 4. Electrochemical and battery cycling performance. a) Galvanostatic cycling of symmetric cells with Li metal and D-Li at 1.0 and 5.0 mA cm^{-2} with energy density of 1.0 and 5.0 mAh cm^{-2}, respectively. c,d) The enlarged voltage profiles of 0–10th (c) and 380–390th hours (d). b) Voltage profile of the first cycle at 1.0 mA cm^{-2} with energy density of 1.0 mAh cm^{-2}. e) Battery cycling performance using NMC811 as cathode material at 1.0 C. The loading of NCM811 is 6.5 mg cm^{-2}. The battery was cycled at 0.1 C for four cycles before cycling at 1.0 C.

capacity gradually decreased to about 131.8 mAh g^{-1} under 1.0 C at 350th cycle. Then it quickly dropped to 74.2 mAh g^{-1} with a capacity retention of only 42.5% after 500 cycles. In contrast, the battery with D-Li exhibited an initial discharge capacity of 193.4 mAh g^{-1} with CE of 82.1% at 0.1 C (red). Then a capacity of 175.4 mAh g^{-1} at 1.0 C was achieved along with a relatively stable capacity plateau, which was better than the Li metal until 350 cycles. A reliable capacity was still received even after long 500 cycles, which is much higher than the Li metal.

Cycling performance of the battery coupled with a high mass loading of ≈20.5 mg cm^{-2} $LiNi_{0.8}Co_{0.15}Al_{0.05}O_2$ (NCA) was investigated (**Figure 5**a,b). It is seen that the battery with D-Li showed a specific capacity of 182.3 mAh g^{-1} with CE of 89.3% at 0.1 C. After 200 cycles, a high capacity of 142.7 mAh g^{-1} with 83.7% capacity retention at 0.2 C remained. However, the capacity of the battery with pure Li metal was decreased to only 25.6 mAh g^{-1} after 55 cycles at 0.2 C. Electrochemical impedance spectroscopy (EIS) was applied to check the interface resistance of the electrode. As shown in Figure 5c, a similar contact resistance of ≈4.3 Ω with both Li metal and D-Li was obtained. However, the battery with D-Li showed a lower charge transfer resistance of ≈13.5 Ω than pure Li metal of ≈17.3 Ω. After 100 cycles, the battery with D-Li displayed a much lower charge transfer resistance of ≈49.6 Ω than the pure Li metal of ≈127.3 Ω. The similar trend particularly with transfer resistance after cycling was also received in symmetric cells (Figure S10a,b, Supporting Information). The largely reduced charge transfer resistance of the battery with D-Li was attributed to the formed thinner SEI layer during cycling.

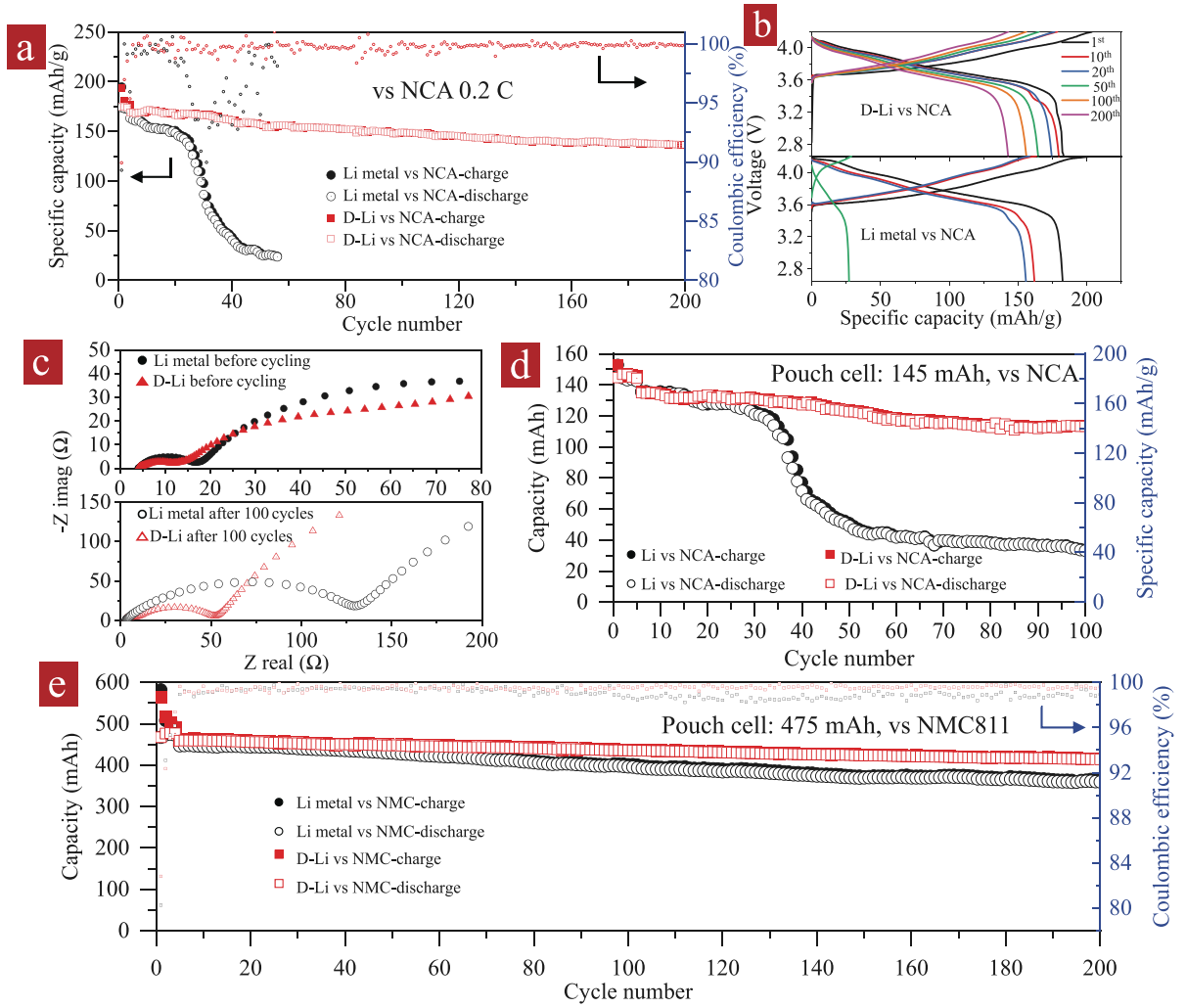

Figure 5. Coin cell and pouch cell battery cycling performance. a) Cycling performance and b) corresponding charge/discharge profiles of the battery versus NCA at 0.2 C. The NCA loading is 20.5 mg cm^{-2}. The battery was cycled at 0.1 C for four cycles before cycling at 0.2 C. c) Nyquist plots of the battery with NCA before and after 100 cycles at 0.2 C. d,e) Pouch cell performance paired with NCA at 0.2 C with a capacity of 145 mAh (d) and paired with NMC811 at 0.5 C with a capacity of 475 mAh (e).

Full pouch cells paired with NCA and NMC811 with a total capacity of 145 and 475 mAh were assembled, respectively. As observed in Figure 5d, both batteries with Li metal and D-Li as anode and NCA as cathode displayed a similar initial capacity of about 145.0 mAh at 0.1 C. Yet, the battery with D-Li still maintained 84.0% capacity after 100 cycles while the capacity of the Li-metal battery dropped to less than 50.0 mAh after 50 cycles. Pouch cells paired with NMC811 with a total capacity of 475 mAh were also used to check the cycling performance. The cell with D-Li showed 94.9% capacity retention after 100 cycles at 0.5 C while the cell with pure Li metal only showed 88.6% capacity retention (Figure 5e). After 200 cycles, the cell with D-Li still had a high-capacity retention of 90.2% while the capacity retention of the cell with Li metal decreased to 80.5%.

The improved battery cyclability is benefited from the reliable lithium deposition and extraction on the dual-layered modified lithium-metal surface. The in-situ-formed honeycomb-like lithium carboxylate flakes act as a pre-formed artificial SEI layer along with the monolayer MXene matrix to provide plenty of active sites for lithium nucleation. The BF_3 doping further reduces the nucleation barrier and increases the electrolyte wettability due to the lithiophilic property. Also the 2D configuration of MXene ensures an excellent conductivity and better regulation of the horizontal growth of lithium. As a result, a thin SEI layer with less inorganic-rich components is formed, which leads to a homogenous growth of lithium without dendrites upon charging/discharging.

3. Conclusion

We have developed a dual-layer interphase that consists of an organic lithium carbonate salt and a BF_3-doped monolayer MXene on the surface of lithium metal, which greatly improves the interfacial stability between lithium metal and plated/stripped lithium by creating more lithiophilic sites and thin artificial SEI layer. The increased surface area and electrolyte wetting further reduce the risk of enlarged local current density, thus preventing the formation of dendrites. The uniform lithium plating and stripping on the anode led to a long cycling capability of large-sized full-cell batteries paired with high-capacity NMC811 and NCA. Particularly the battery paired with NMC811 exhibited a stable capacity retention over 500 cycles. A pouch cell with a capacity of 475 mAh exhibited >90.2% capacity retention after long 200 cycles. Commercially available coating process such as spray or dip coatings can be applied to form the dual-layer interphase, which provides a scalable way to achieve high energy-density Li-metal batteries in powering large devices such as EVs.

4. Experimental Section

Synthesis of D-Li: Ti_3C_2 MXene was synthesized through etching of Ti_3AlC_2 MAX (400 mesh, Lizhou Kai Kai Ceramic Materials) by hydrofluoric acid.[18] In a typical experiment, 3.0 g of MAX precursor was slowly added into 30 mL of HF solution (48–52%, Sigma-Aldrich) in a Teflon container (Baoshishan) under magnetic stirring (Magnetic Stirrer, RT Basic-17, Thermo Scientific). After stirring for 1 h at room temperature, the container was placed in a water bath and kept stirring for 24 h at 60 °C (Stirring Hot Plate, Thermo Scientific Cimarec). After centrifuging (Compact Centrifuge, model 6755, Corning LSE) and washing using de-ionized water until reaching a pH of ≈6 (pH Test Strips, VWR Chemicals BDH), the sediment was collected via vacuum-assisted filtration (Vacuum Filtration System, VWR) using a polyvinyl difluoride (PVDF) filter membrane with a pore size of 0.22 µm (EZFlow, 364-2612-OEM) and dried in a vacuum oven (Ai 0.9, Across International) at 80 °C for 24 h. To obtain the monolayer MXene dispersion, 0.1 g of as-received MXene was dispersed in 25 wt% tetrabutylammonium hydroxide solution (40% in water, Sigma-Aldrich) and stirred for 6 h at room temperature. The mixture was centrifuged and washed with ethanol (200 proof) for three times, followed by dispersing in 50 mL of THF (anhydrous, 99.9%, Sigma-Aldrich) solvent. The obtained solution was sealed in a container and agitated by an ultrasound cleaner (Symphony, VWR) for 10 h. Then the monolayer MXene dispersion was collected after centrifuging at 2500 rpm for 30 min. 2.0 vol% of boron trifluoride THF complex (BF_3 concentration of 47.5–49.5%, Sigma-Aldrich) was added into the monolayer MXene dispersion in THF. After stirring for 24 h, the BF_3-MXene dispersion was obtained. All the coating and drying procedures were performed in an Ar filled glovebox (H_2O < 0.5 ppm; O_2 < 0.1 ppm, Mbraun, Labstar Pro). Before coating, pure Li metal (for coin cells: 0.25 mm, 99.9%, TMAX, China; for pouch cells: lithium on Cu, Li: 30–50 µm, Cu: 8–12 µm, China Energy Lithium Co. Ltd) was carefully cleaned to remove the surface impurities by using brush. 0.15 vol% of pentanoic acid (≥99%, Sigma-Aldrich) was uniformly dispersed into THF solvent under agitation. 30 µL of pentanoic acid solution was dropped on the Li-metal surface, followed by drying on a hot plate (Stirring Hot Plate, Thermo Scientific Cimarec) at 25 °C for 30 min. To control the MXene amount for coin cells, 30 µL of BF_3-MXene solution was dropped on the Li-metal surface, which was repeated three times after drying. For pouch cells, a spray coating method was applied with a solution to area ratio of ≈45 µL cm^{-2}. The D-Li anode electrode was finally obtained after drying at 25 °C for 24 h.

Electrochemical Measurements: *Coin cell assembly*: Symmetric cells (CR2032, Xingye Co., Ltd.) were assembled by using pure Li or the prepared D-Li as both electrodes in an Ar filled glovebox (H_2O < 0.5 ppm; O_2 < 0.1 ppm, Mbraun, Labstar Pro). The electrolyte was 1.0 M lithium bistrifluoromethane sulfonimide (BASF Corp.) in 1,3-dioxolane/DME (BASF Corp.) with a 1:1 volume ratio and 0.1 M $LiNO_3$ (99.99%, Sigma-Aldrich) as an additive. The electrolyte amount was controlled to ≈30 µL/coin cell. For full-cell batteries, NCA was directly obtained from a brand new 18650 cylindrical battery (35E, Samsung, the NCA mass loading was 20.5 mg cm^{-2} for single side and 41.0 mg cm^{-2} for double sides). NMC811 was prepared through a modified coprecipitation method based on our previous work.[42] To make a slurry, the active material, conductive carbon (SuperP, C65, Timcal), and PVDF (laboratory grade, Alfa Aesar) with a weight ratio of 80:10:10 were mixed in *N*-methyl-2-pyrrolidone (NMP, 99.9%, Headspace Solvents, Honeywell). Then the as-received slurry was coated on a carbon coated Al foil (18 µm, 99.3%, MTI Corp.) and dried in a vacuum oven (Vacuum oven, Ai 0.9, Across International) at 60 °C for 12 h. After pressed at 6–10 MPa by a benchtop hydraulic press (Northern Tool+ Equipment), the electrode was pouched into a circle disc using a disc cutter (MSK-T-07, MTI Corp.). By using the prepared cathode electrode, polyethylene separator (Celgard 2400), and pure lithium-metal foil (99.9%, TMAX) or D-Li, a stainless-steel coin cell was assembled inside the Ar-filled glovebox. The electrolyte was 1.0 M $LiPF_6$ (battery grade, >99.99% trace metals basis, Sigma-Aldrich) in the solvent of ethylene carbonate (EC) (battery grade, BASF Corp.) and ethyl methyl carbonate (EMC) (battery grade, BASF Corp.) with 3:7 volume ratio and 2 wt% vinylene carbonate (VC) (99.5%, battery grade, Sigma-Aldrich).

Pouch cell assembly: Full pouch cells with total capacities of 145 and 475 mAh were assembled using NCA and NMC811 as cathode materials, respectively. Double-side coated NCA electrode with area of 4 × 5 cm^2 was obtained from an 18650 cylindrical battery (35E, Samsung) with a total mass loading of 41.0 mg cm^{-2}. To obtain the

145 mAh pouch cell, a sandwich structure with one double-side coated NCA electrode coupled with two pieces of pure Li or D-Li on Cu foil (lithium on Cu, Li: 30–50 µm, Cu: 8–12 µm, China Energy Lithium Co. Ltd) was assembled. To make the NMC811 slurry for pouch cells, the active material, conductive carbon (SuperP, C65, Timcal) and PVDF (laboratory grade, Alfa Aesar) with the weight ratio of 93.5:4.0:2.5 were uniformly mixed in NMP (99.9%, Headspace Solvents, Honeywell). Then the received slurry was coated on a carbon coated Al foil (18 µm, 99.3%, MTI Corp.) and dried using an automatic compact tape casting coater with heat (BNP-TMD1, BONAPU). The electrode was double-side coated with a total mass loading of 25 mg cm^{-2}. After calendaring by a cold roller (BNP-DG100DL, BONAPU), the electrode was cut into small pieces of 4×5 cm^2. To assemble the 475 mAh pouch cell, five layers of double-side coated NMC811 on Al foil were used as cathode and six layers of pure Li metal or D-Li (30–50 µm, China Energy Lithium Co. Ltd) on Cu foil as anode. The Celgard 2400 microporous PE membrane was used as the separator. The Ni and Al tabs with 3 mm width (MTI Corp.) were used for anode and cathode connections via an ultrasonic metal spot welding machine (TMAX-USW-2000 W, 40 Hz, TMAX Battery Equipment). Electrolyte was 1.0 M $LiPF_6$ in 3:7 volume ratio of EC and EMC with 2 wt% VC as additive. The electrolyte amount was 6.0 g A^{-1} h^{-1} on the basis of cathode capacity. The cell was sealed by using a pouch-cell vacuum sealing machine (TMAX-YF, TMAX Battery Equipment).

Capillary cell assembly: The capillary cell was made by a sealed transparent hourglass-type tube. The inner diameter of the middle tube for observation was 3 mm, which was connected with two tubes with a diameter of 4 mm. Symmetric cells with D-Li or pure Li metal were closed inside the capillary cell in the Ar-filled glovebox. A copper wire with a diameter of 1.0 mm (99%, Fisher Scientific) was used as current collector and was connected to the battery tester. The electrolyte was 1.0 M $LiPF_6$ in the solvent of EC and EMC with 3:7 volume ratio and 2 wt% VC. The current density was controlled by using a battery tester system (LANDT 2001CT, Landt Instruments, Inc.). A digital trinocular stereo zoom microscope (SM-3TZ-54S-5 M, AmScope) was used to record the surface morphology change upon Li stripping/platting.

Electrochemical property and battery performance measurements: The EIS in the frequency range of 0.01–10^5 Hz was checked by using Gamry 600+ Potentiostat/Galvanostat/ZRA. The EIS of the full cell with NCA was checked at a charged state of 4.2 V. The EIS for symmetric cells was checked upon stripping after cycling. The galvanostatic cycling performance of the assembled batteries was measured by a battery tester system (LANDT 2001CT, Landt Instruments, Inc.) after resting 4 h at room temperature. Cycling performance of the symmetric cells was checked with current densities of 1 and 5 mA cm^{-2} with energy densities of 1 and 5 mAh cm^{-2}, respectively. All the full coin cells and pouch cells were subjected to activation of four charge/discharge cycles at 0.1 C with voltage window of 2.62–4.2 V for NCA and 2.8–4.3 V for NMC811.

Sample Characterizations: The sample morphology was checked by using Hitachi S4800 ultrahigh resolution field emission SEM. Thermo Scientific ESCALAB 250Xi equipped with electron flood gun and scanning ion gun with an Al Kα line (photon energy: 1486.6 eV) of a non-monochromatic X-ray source was used to perform the XPS measurement. An ultrahigh vacuum apparatus with a base pressure below 1×10^{-10} Pa was used to collect the spectra, where the angle between the hemispherical analyzer and the sample surface was 45°. Prior to XPS measurements, the sample was cycled for three times in a symmetric cell at 1.0 mA cm^{-2} with a capacity of 1.0 mAh cm^{-2}. The electrode material was collected at stripping state and rinsed with DME solvent (BASF Corp.) to remove the electrolyte residuals. After drying at room temperature in glovebox, the electrode sample was sealed with Ar before being transferred into the XPS spectrometer chamber. XPS depth profile was checked with X-ray spot size of 500 µm after etching for different time by using Ar ion sputter gun at 2 kV. The sputter rate was controlled to be ≈0.3 nm s^{-1}. All acquired spectra were calibrated using standard C 1s peak at 284.8 eV.

Supporting Information

Supporting Information is available from the Wiley Online Library or from the author.

Acknowledgements

Material preparation, battery assembly, and tests were carried out at the University of Wisconsin-Milwaukee (UWM). SEM measurements were completed at the Advanced Analysis Facility (AAF), UWM. The XPS including depth profiling analysis was done by using the facility of NUANCE Center at the Northwestern University. All authors acknowledge the supports from the NSF grant #2013525 and the UW System Ignite Grant Program under award #FY21-Y-106-068000-4.

Conflict of Interest

The authors declare no conflict of interest.

Author Contributions

J.J.N. conceived the project. M.S. synthesized the samples and performed the characterizations and battery performance tests. J.J.N. and M.S. wrote the manuscript. All authors participated in the data discussion.

Data Availability Statement

The data that support the findings of this study are available from the corresponding author upon reasonable request.

Keywords

anodes, batteries, doping, lithium metal, MXenes

Received: November 1, 2022
Revised: December 7, 2022
Published online:

[1] X. B. Cheng, R. Zhang, C. Z. Zhao, Q. Zhang, *Chem. Rev.* **2017**, *117*, 10403.
[2] K. N. Wood, E. Kazyak, A. F. Chadwick, K. H. Chen, J. G. Zhang, K. Thornton, N. P. Dasgupta, *ACS Cent. Sci.* **2016**, *2*, 790.
[3] X. Y. Zhang, A. X. Wang, X. J. Liu, J. Y. Luo, *Acc. Chem. Res.* **2019**, *52*, 3223.
[4] R. Zhang, X. R. Chen, X. Chen, X. B. Cheng, X. Q. Zhang, C. Yan, Q. Zhang, *Angew. Chem., Int. Ed.* **2017**, *56*, 7764.
[5] K. Yan, J. Y. Wang, S. Q. Zhao, D. Zhou, B. Sun, Y. Cui, G. X. Wang, *Angew. Chem., Int. Ed.* **2019**, *58*, 11364.
[6] X. R. Chen, B. C. Zhao, C. Yan, Q. Zhang, *Adv. Mater.* **2021**, *33*, 2004128.
[7] C. B. Jin, T. F. Liu, O. W. Sheng, M. Li, T. C. Liu, Y. F. Yuan, J. W. Nai, Z. J. Ju, W. K. Zhang, Y. J. Liu, Y. Wang, Z. Lin, J. Lu, X. Y. Tao, *Nat. Energy* **2021**, *6*, 378.
[8] X. D. Ren, L. F. Zou, S. H. Jiao, D. H. Mei, M. H. Engelhard, Q. Y. Li, H. Y. Lee, C. J. Niu, B. D. Adams, C. M. Wang, J. Liu, J. G. Zhang, W. Xu, *ACS Energy Lett.* **2019**, *4*, 896.

[9] C. Y. Cui, C. Y. Yang, N. Eidson, J. Chen, F. D. Han, L. Chen, C. Luo, P. F. Wang, X. L. Fan, C. S. Wang, *Adv. Mater.* **2020**, *32*, 1906427.
[10] Y. M. Zhao, G. X. Li, Y. Gao, D. W. Wang, Q. Q. Huang, D. H. Wang, *ACS Energy Lett.* **2019**, *4*, 1271.
[11] X. J. Liu, J. Liu, T. Qian, H. L. Chen, C. L. Yan, *Adv. Mater.* **2020**, *32*, 1902724.
[12] C. A. Calderon, A. Vizintin, J. Bobnar, D. E. Barraco, E. P. M. Leiva, A. Visintin, S. Fantini, F. Fischer, R. Dominko, *ACS Appl. Energy Mater.* **2020**, *3*, 2020.
[13] P. B. Zhai, L. X. Liu, Y. Wei, J. H. Zuo, Z. L. Yang, Q. Chen, F. F. Zhao, X. K. Zhang, Y. J. Gong, *Nano Lett.* **2021**, *21*, 7715.
[14] D. Zhang, A. Dai, B. F. Fan, Y. G. Li, K. Shen, T. Xiao, G. Y. Hou, H. Z. Cao, X. Y. Tao, Y. P. Tang, *ACS Appl. Mater. Interfaces* **2020**, *12*, 31542.
[15] Z. Liang, K. Yan, G. M. Zhou, A. Pei, J. Zhao, Y. M. Sun, J. Xie, Y. B. Li, F. F. Shi, Y. Y. Liu, D. C. Lin, K. Liu, H. S. Wang, H. X. Wang, Y. Y. Lu, Y. Cui, *Sci. Adv.* **2019**, *5*, eaau5655.
[16] Z. Shadike, H. Lee, O. Borodin, X. Cao, X. L. Fan, X. L. Wang, R. Q. Lin, S. M. Bak, S. Ghose, K. Xu, C. S. Wang, J. Liu, J. Xiao, X. Q. Yang, E. Y. Hu, *Nat. Nanotechnol.* **2021**, *16*, 549.
[17] X. H. Shen, S. Shi, B. L. Li, S. Y. Li, H. M. Zhang, S. Chen, H. L. Deng, Q. S. Zhang, J. Zhu, X. D. Duan, *Adv. Funct. Mater.* **2022**, *32*, 2206388.
[18] Y. Y. Pei, X. L. Zhang, Z. Y. Hui, J. Y. Zhou, X. Huang, G. Z. Sun, W. Huang, *ACS Nano* **2021**, *15*, 3996.
[19] M. Naguib, M. Kurtoglu, V. Presser, J. Lu, J. J. Niu, M. Heon, L. Hultman, Y. Gogotsi, M. W. Barsoum, *Adv. Mater.* **2011**, *23*, 4248.
[20] M. W. Shang, X. Chen, B. X. Li, J. J. Niu, *ACS Nano* **2020**, *14*, 3678.
[21] Y. L. Zhang, Z. J. Mu, J. P. Lai, Y. G. Chao, Y. Yang, P. Zhou, Y. J. Li, W. X. Yang, Z. H. Xia, S. J. Guo, *ACS Nano* **2019**, *13*, 2167.
[22] X. B. Hui, R. Z. Zhao, P. Zhang, C. X. Li, C. X. Wang, L. W. Yin, *Adv. Energy Mater.* **2019**, *9*, 1901065.
[23] Y. L. An, Y. Tian, C. K. Liu, S. L. Xiong, J. K. Feng, Y. T. Qian, *ACS Nano* **2022**, *16*, 4560.
[24] D. Zhang, S. Wang, B. Li, Y. J. Gong, S. B. Yang, *Adv. Mater.* **2019**, *31*, 1901820.
[25] J. A. Gu, Q. Zhu, Y. Z. Shi, H. Chen, D. Zhang, Z. G. Du, S. B. Yang, *ACS Nano* **2020**, *14*, 891.
[26] Q. Chen, Y. Wei, X. K. Zhang, Z. L. Yang, F. Wang, W. Liu, J. H. Zuo, X. K. Gu, Y. Yao, X. G. Wang, F. F. Zhao, S. B. Yang, Y. J. Gong, *Adv. Energy Mater.* **2022**, *12*, 2200072.
[27] Y. Qian, C. L. Wei, Y. A. Tian, B. J. Xi, S. L. Xiong, J. K. Feng, Y. T. Qian, *Chem. Eng. J.* **2021**, *421*, 129685.
[28] J. M. Wang, M. Yang, G. D. Zou, D. Liu, Q. M. Peng, *Adv. Funct. Mater.* **2021**, *31*, 2101180.
[29] Y. Tian, Y. L. An, C. L. Wei, Y. Tao, Y. C. Zhang, H. Y. Jiang, L. Tan, J. Feng, Y. T. Qian, *Chem. Eng. J.* **2021**, *406*, 126836.
[30] X. Chen, M. W. Shang, J. J. Niu, *Nano Lett.* **2020**, *20*, 2639.
[31] S. Schmohl, X. He, H. D. Wiemhofer, *Polymers* **2018**, *10*, 1350.
[32] D. M. Kang, S. Sardar, R. Zhang, H. Noam, J. Y. Chen, L. G. Ma, W. B. Liang, C. S. Shi, J. P. Lemmon, *Energy Storage Mater.* **2020**, *27*, 69.
[33] M. Q. Zhao, X. Q. Xie, C. E. Ren, T. Makaryan, B. Anasori, G. X. Wang, Y. Gogotsi, *Adv. Mater.* **2017**, *29*, 1702410.
[34] K. Maleski, V. N. Mochalin, Y. Gogotsi, *Chem. Mater.* **2017**, *29*, 1632.
[35] H. D. Shi, C. J. Zhang, P. F. Lu, Y. F. Dong, P. C. Wen, Z. S. Wu, *ACS Nano* **2019**, *13*, 14308.
[36] V. Natu, M. Benchakar, C. Canaff, A. Habrioux, S. Celerier, M. W. Barsoum, *Matter* **2021**, *4*, 1224.
[37] Y. W. Xie, H. Y. Zhang, J. L. Yu, Z. J. Liu, S. S. Zhang, H. Y. Shao, Y. L. Cao, X. F. Huang, S. K. Li, *Small* **2022**, *18*, 2104876.
[38] W. Liu, P. B. Zhai, S. J. Qin, J. Xiao, Y. Wei, W. W. Yang, S. Q. Cui, Q. Chen, C. Q. Jin, S. B. Yang, Y. J. Gong, *J. Energy Chem.* **2021**, *56*, 463.
[39] C. K. Chan, H. L. Peng, G. Liu, K. McIlwrath, X. F. Zhang, R. A. Huggins, Y. Cui, *Nat. Nanotechnol.* **2008**, *3*, 31.
[40] Z. Y. Lu, W. T. Li, Y. Long, J. C. Liang, Q. H. Liang, S. C. Wu, Y. Tao, Z. Weng, W. Lv, Q. H. Yang, *Adv. Funct. Mater.* **2020**, *30*, 1907343.
[41] D. C. Lin, Y. Y. Liu, Y. B. Li, Y. Z. Li, A. Pei, J. Xie, W. Huang, Y. Cui, *Nat. Chem.* **2019**, *11*, 382.
[42] M. W. Shang, X. Chen, J. J. Niu, *Cell Rep. Phys. Sci.* **2022**, *3*,100767.

